Supporting Information

Heterogeneous In/Mo cooperative bandgap engineering for promoting visible-light-driven CO_2 photoreduction

Guoyang Gao,[a] Qiuye Wang,[a] Peifen Zhu,*[b] Hongyang Zhu,[c] Yang Qu[a] and Guofeng Wang*[a]

[a]Key Laboratory of Functional Inorganic Material Chemistry, Ministry of Education, School of Chemistry and Materials Science, Heilongjiang University, Harbin 150080, China

[b]Department of Electrical Engineering and Computer Science, University of Missouri, Columbia, MO 65211, USA

[c]School of Physics and Electronic Engineering, Linyi University, Linyi 276005, China

*Corresponding author E-mail: 2010070@hlju.edu.cn (G. Wang), pzhu@missouri.edu (P. Zhu).

Experimental Section

Materials. All reagents used in the experiment were A.R. grade. Deionized water was used throughout the experiment. Indium nitrate ($In(NO_3)_3 \cdot 4.5H_2O$), sodium hydroxide(NaOH), ethanol, and oleic acid were purchased from Sinopharm Chemical ReagentCo., Ltd. Sodium molybdate dihydrate ($Na_2MoO_4 \cdot 2H_2O$) was purchased from Aladdin Industrial Corporation (Shanghai, China).

Characterization. Powder X-ray diffraction (XRD) patterns were recorded on a Bruker D8 diffractometer using Cu Kα (λ=1.5406 Å) radiation with accelerating voltage 40 kV. Fourier transform infrared (FT-IR) spectra were acquired on a Perkin-Elmer Spectrum One FTIR spectrometer using the KBr pellet method. UV–vis spectra were obtained by using a UV-visible spectrophotometer (SHIMADZU UV-2550) within a wavelength range of 200-800 nm. Transmission electron microscopy (TEM) measurements were carried out on a JEM-2100 electron microscope (JEOL, Japan) with an acceleration voltage of 200 kV. Scanning electron microscopy (SEM) measurements and energy dispersive X-ray spectroscopy (EDX) elemental mapping characterization were performed on a Hitachi S-4800 at an accelerating voltage of 5 kV. X-ray photoelectron spectroscopy (XPS) with a VG ESCALAB MK II (Mg Ka, 1253.6 eV) was used to confirm the chemical circumstance of the elements. Thermogravimetric analysis (TGA) was carried out in an air atmosphere, from 20 °C to 800 °C by using a thermal analyzer (TGA-7, Perkin-Elmer, USA). Raman spectra measurements were performed on a Jobin Yvon HR 800 micro-Raman spectrometer at 460 nm. The N_2 adsorption and desorption isotherms (BET) were analyzed with Tristar II 3020. The pore size distribution charts were obtained by the Barrett-Joyner-Halenda (BJH) method.

Photoelectrochemical measurement. Photochemical measurements were performed by using a CHI-660 electrochemical workstation (Chenhua Instrument, Shanghai, China) with a 300W Xe arc lamp as the light source. A conductive fluorine-doped tin oxide (FTO) coated glass was

used as the substrate, and the sample was made into a thin film as a working electrode. The working electrode was prepared as follows: 0.1 g sample was dissolved in 1 mL isopropanol, and subsequently, the solution was mixed with 0.05 g Macrogol-2000. The entire process was performed under vigorous stirring and thoroughly mixed using ultrasonic assistance for 10 minutes. The suspension was kept under vigorous stirring for 30 minutes, and then 0.05 ml acetylacetone was added to the above mixture. The obtained solution was kept under stirring for one week. This mixture was coated on a 1 cm × 1 cm FTO glass electrode by a doctor blade method as an effective surface area. Finally, the electrode was dried at room temperature. Pt foil and Ag/AgCl (saturated KCl) were used as the counter electrode and the reference electrode, respectively. A 0.5 M Na_2SO_4 aqueous solution was used as the electrolyte.

Hydroxyl radical (·OH) measurement. This test was used to analyze the amount of ·OH produced during the photocatalytic reaction. Typically, 50 mg of the product was dissolved in 40 ml coumarin aqueous solution (0.001 M), and the solution was thoroughly stirred for 10 minutes, and irradiated with a 300W Xenon lamp for 1 h. The final product was separated by centrifugation. The supernatant was added to the cuvette and analyzed by using a Hitachi F-4600 fluorescence spectrophotometer (λ_{ex} = 390nm).

Photocatalytic measurement. The photocatalytic performances of the samples were evaluated by visible-light-driven CO_2 reduction. Typically, 0.020 g of powder sample was dispersed in 4 mL of water with constant stirring and then transferred to a 100 mL cylindrical steel reactor with a quartz window (3.5 cm^2). Before irradiation, high-purity CO_2 (99.999%) was passed to the reaction system to sufficiently remove air and establish an equilibrium of adsorption and desorption. A 300W Xenon lamp (PLSSXE300 / 300UV, Beijing) with a 420 nm cut-off filter was used as the light source and the light intensity was 420 mW/cm^2. The entire reaction was performed at room temperature with continuous stirring. Finally, the gas generated by the

reaction was detected by using gas chromatography (GC2002). The photocatalytic reaction of the same sample was performed five times, and the test data were averaged.

Computational Details. The first-principles calculations were performed based on density functional theory (DFT) implemented in the Vienna ab-initio simulation package (VASP) [1-3]. The electron-ion interaction was described by the projector augmented wave (PAW) method [4]. The generalized gradient approximation (GGA) with the Perdew-Burke-Ernzerhof (PBE) exchange-correlation functional was used in the calculations [5]. The band structure, density of states (DOS), work function, and charge density difference were simulated with the plane-wave ultrasoft (PWUS) pseudopotential method as implemented in the MedeA-VASP [6]. The cutoff energy for the plane-wave expansion was set to 500 eV. For geometry optimization, the convergence criterion of total energy was 1.0×10^{-5} eV/atom. The force tolerance for the structure optimization is 0.02 eV/Å. The spin-polarized magnetic calculation was used to do geometry optimization, electronic structure, and optical property calculation. The spacing of k points was set to 0.2/Å. The charge density difference (also called deformation charge density) was obtained by taking the difference between the self-consistent pseudo charge density and the superposition of atomic charge densities. The real (ε_r) and imaginary (ε_i) parts of complex dielectric constants ($\varepsilon_{complex}$) were extracted from VASP calculation: $\varepsilon_{complex}(\omega) = \varepsilon_r(\omega) + i\varepsilon_i(\omega)$, where ω is the angular frequency of light. The complex optical conductivity was defined as $\sigma_{complex}(\omega) = \sigma_r(\omega) + i\sigma_i(\omega)$. The real part of optical conductivity was calculated as $\sigma_r(\omega) = \frac{\varepsilon_o\varepsilon_i\omega}{4\pi}$ and imaginary part of optical conductivity was calculated as $\sigma_i(\omega) = \frac{\varepsilon_o\varepsilon_r\omega}{4\pi}$, where ε_o is permittivity in free space. The complex refractive index was defined as $n_{complex}(\omega) = n(\omega) + ik(\omega)$. The real part of the refractive index was calculated as $n(\omega) = \left[\left(\varepsilon_r^2 + \varepsilon_i^2\right)^{\frac{1}{2}} + \varepsilon_r^2\right]^{\frac{1}{2}}$ and the imaginary part of refractive index (extinction coefficient) was

calculated as $k(\omega) = \left[\left(\varepsilon_r^2 + \varepsilon_i^2\right)^{\frac{1}{2}} - \varepsilon_r^2\right]^{\frac{1}{2}}$. The absorption coefficient was calculated as $\alpha_{abs}(\omega) = 2\frac{\omega k(\omega)}{c}$, where c is the speed of light in a vacuum.

To investigate the effect of Mo doping on the properties of InOOH, a 2x2x2 supercell was created and a different number of In was then replaced with Mo. The structure optimization was carried out for the newly created structures. The band unfolding technique was employed to study the effect of Mo the bandstructure modification.

Reference:

[1] G. Kresse, J. Hafner, Ab initio molecular dynamics for open-shell transition metals, Phys. Rev. B, 48 (1993) 13115-13118.

[2] G. Kresse, J. Furthmüller, Efficiency of ab-initio total energy calculations for metals and semiconductors using a plane-wave basis set, Comput. Mater. Sci., 6 (1996) 15-50.

[3] G. Kresse, J. Furthmüller, Efficient iterative schemes for ab initio total-energy calculations using a plane-wave basis set, Phys. Rev. B, 54 (1996) 11169-11186.

[4] G. Kresse, D. Joubert, From ultrasoft pseudopotentials to the projector augmented-wave method, Phys. Rev. B, 59 (1999) 1758-1775.

[5] J.P. Perdew, K. Burke, M. Ernzerhof, Generalized Gradient Approximation Made Simple, Phys. Rev. Lett., 77 (1996) 3865-3868.

[6] https://www.materialsdesign.com/products.

Table S1. The fitted results of Nyquist plots for $In(OH)_3$, InOOH, IOOH/IOH-20 and Mo-IOOH/IOH-20. (R_{ct} is the charge transfer resistance, and R_s is the solution resistance.)

Sample	R_s (Ω)	R_{ct} (Ω)
$In(OH)_3$	69.53	772.8
InOOH	66.6	468.1
IOOH/IOH-20	67.58	325.2
Mo-IOOH/IOH-20	69.93	98.97

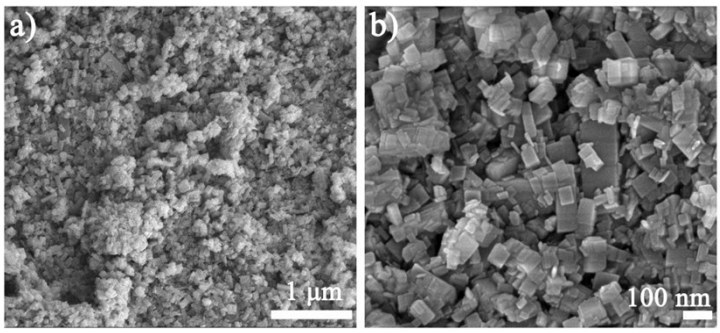

Figure S1. SEM images of $In(OH)_3$.

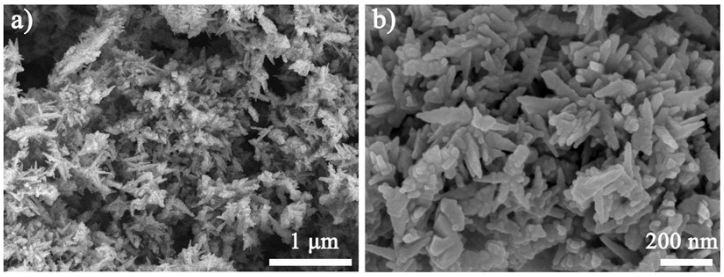

Figure S2. SEM images of InOOH.

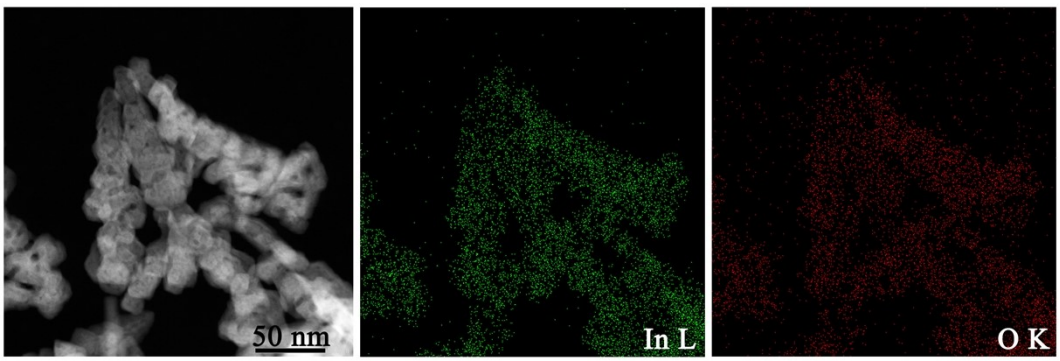

Figure S3. HAADF-STEM image and EDS elemental mappings of InOOH.

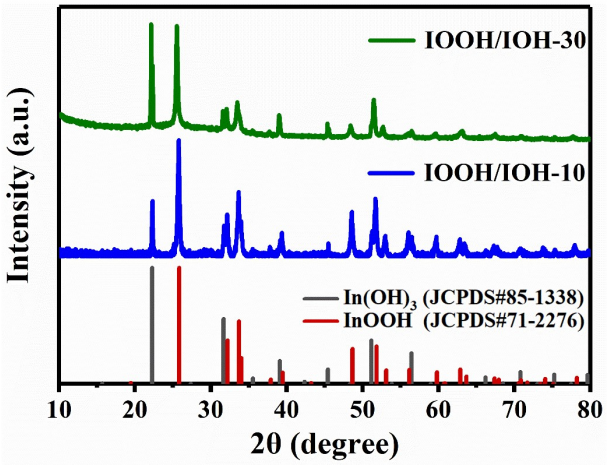

Figure S4. XRD patterns of IOOH/IOH-10 and IOOH/IOH-30.

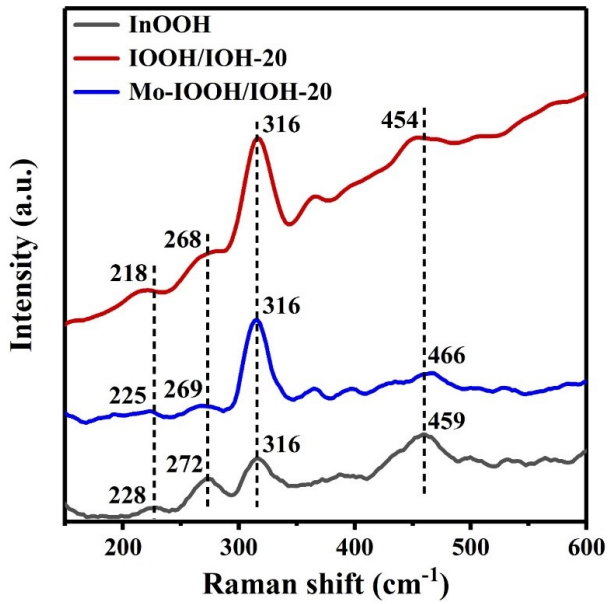

Figure S5. Raman spectra of InOOH, IOOH/IOH-20, and Mo-IOOH/IOH-20.

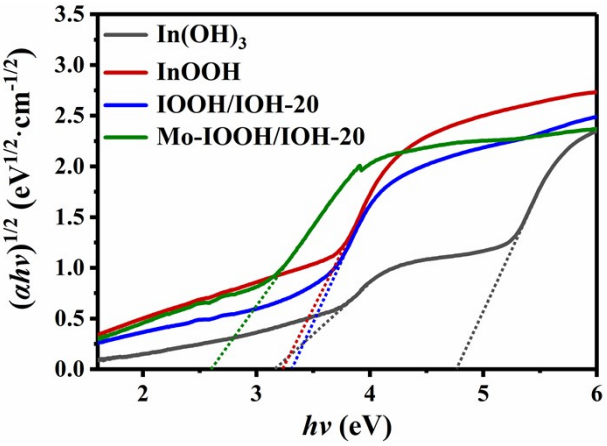

Figure S6. Bandgaps plots of $In(OH)_3$, InOOH, IOOH/IOH-20, and Mo-IOOH/IOH-20.

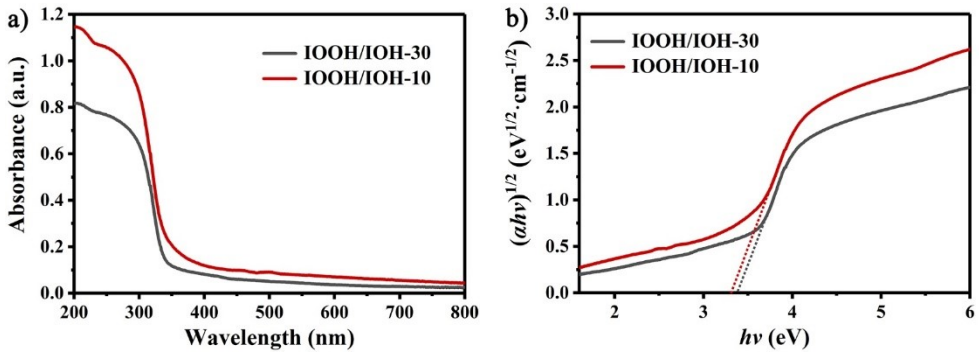

Figure S7. (a) UV-vis diffuse reflectance spectra and (b) bandgaps plots of IOOH/IOH-10 and IOOH/IOH-30.

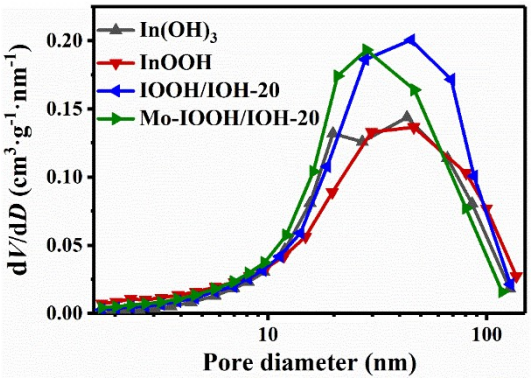

Figure S8. The pore size distributions of $In(OH)_3$, InOOH, IOOH/IOH-20, and Mo-IOOH/IOH-20.

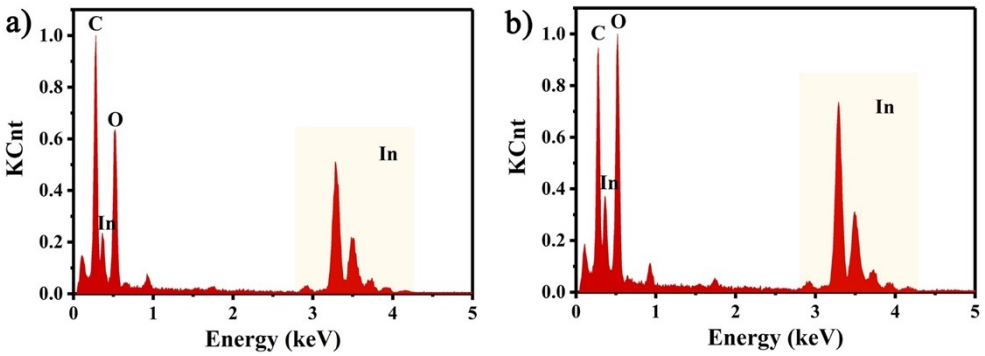

Figure S9. EDS spectra of (a) $In(OH)_3$ and (b) InOOH.

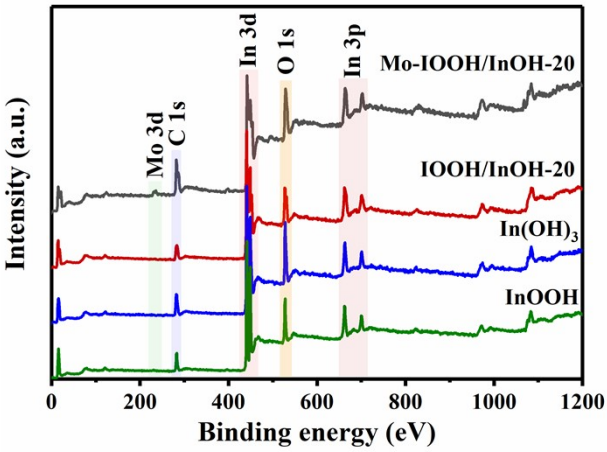

Figure S10. XPS survey spectra of $In(OH)_3$, InOOH, IOOH/IOH-20, and Mo-IOOH/IOH-20.

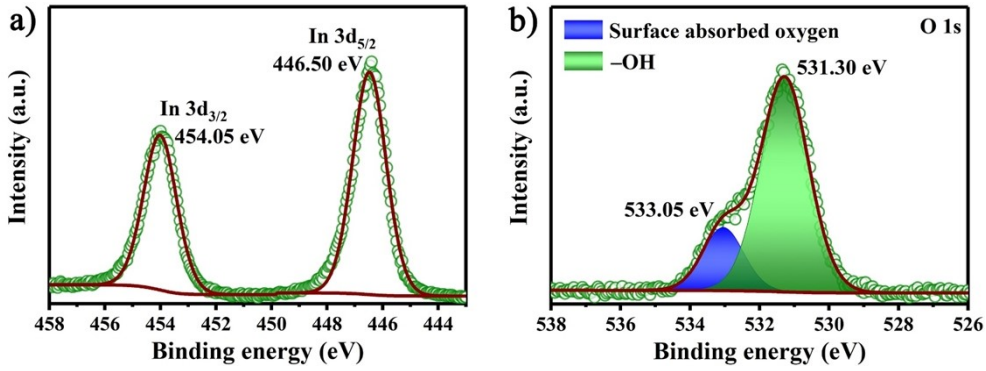

Figure S11. XPS spectra for $In(OH)_3$ in regions of (a) In 3d and (b) O 1s.

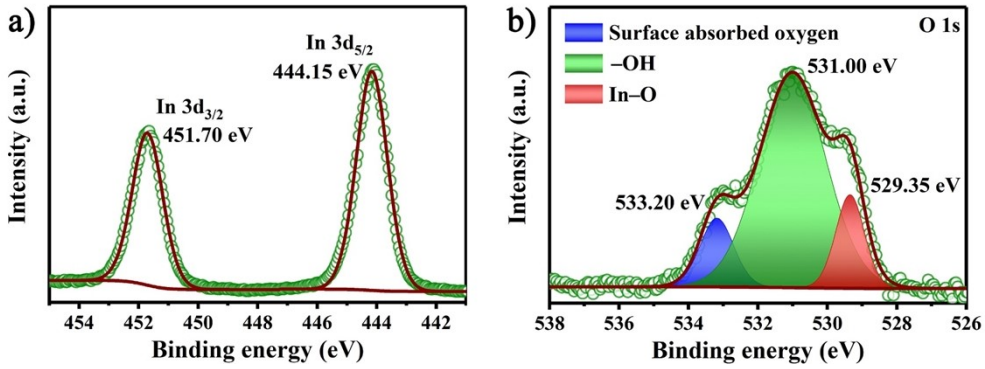

Figure S12. XPS spectra for InOOH in regions of (a) In 3d and (b) O 1s.

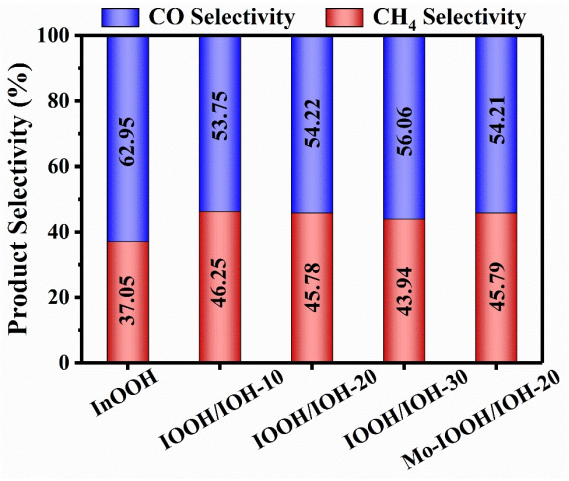

Figure. S13 Products selectivity of InOOH, IOOH/IOH-10, IOOH/IOH-20, IOOH/IOH-30, Mo-IOOH/IOH-10.

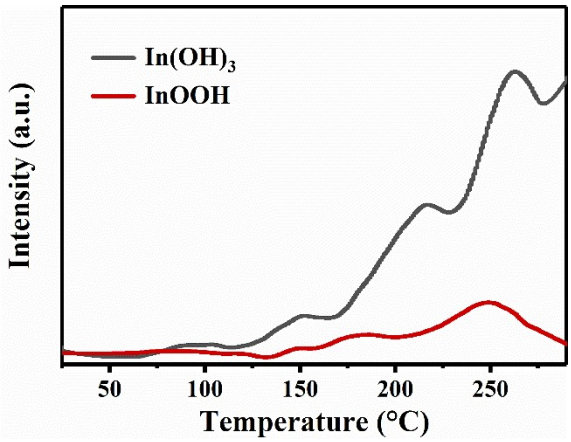

Figure S14. CO_2-TPD plots of $In(OH)_3$ and InOOH.

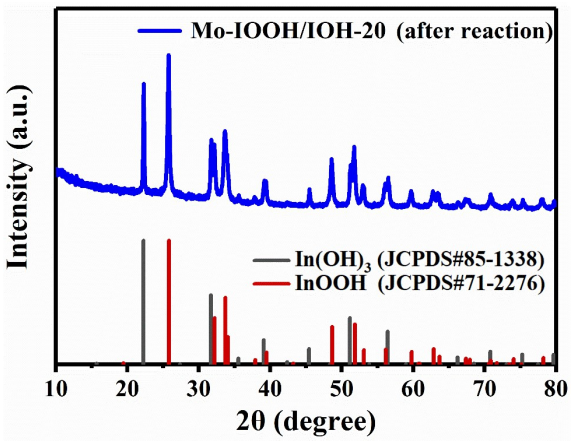

Figure S15. XRD pattern of Mo-IOOH/IOH-20 after the photocatalytic reaction.

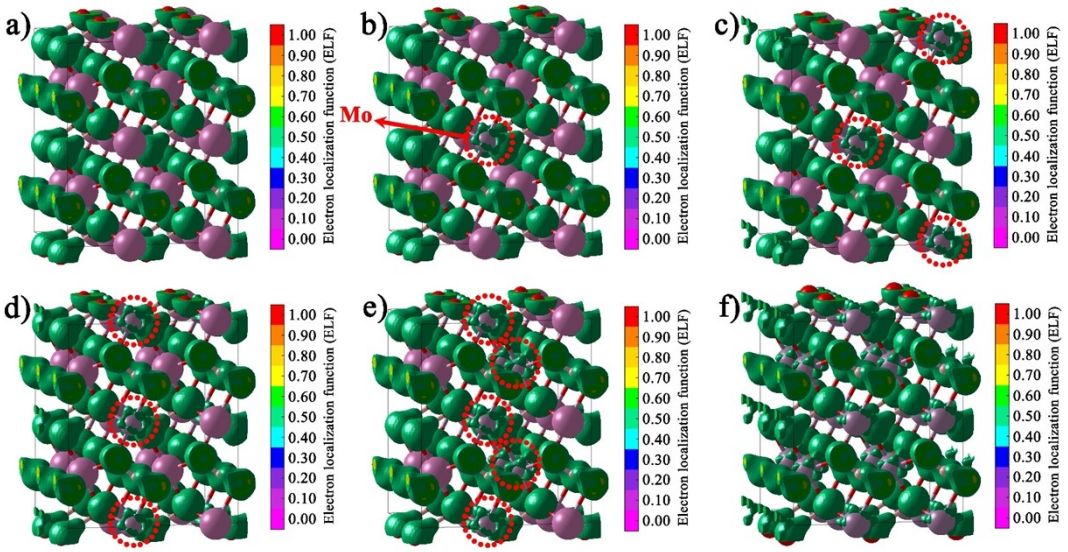

Figure S16. The electron localization function (ELF) of (a) $In_{16}H_{16}O_{32}$, (b) $MoIn_{15}H_{16}O_{32}$, (c) $Mo_2In_{14}H_{16}O_{32}$, (d) $Mo_4In_{12}H_{16}O_{32}$,(e) $Mo_8In_8H_{16}O_{32}$, and (f) $Mo_{16}H_{16}O_{32}$.

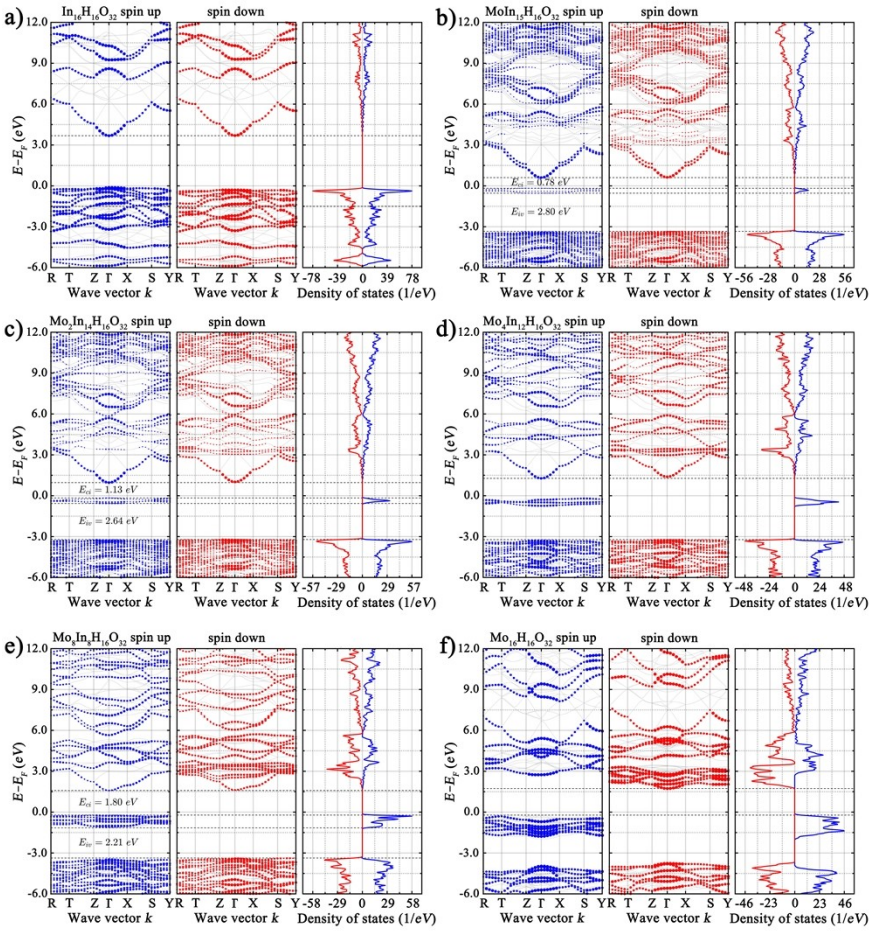

Figure S17. Theoretical simulation of band structure and density of states for (a) $In_{16}H_{16}O_{32}$, (b) $MoIn_{15}H_{16}O_{32}$, (c) $Mo_2In_{14}H_{16}O_{32}$, (d) $Mo_4In_{12}H_{16}O_{32}$, (e) $Mo_8In_8H_{16}O_{32}$, and (f) $Mo_{16}H_{16}O_{32}$.

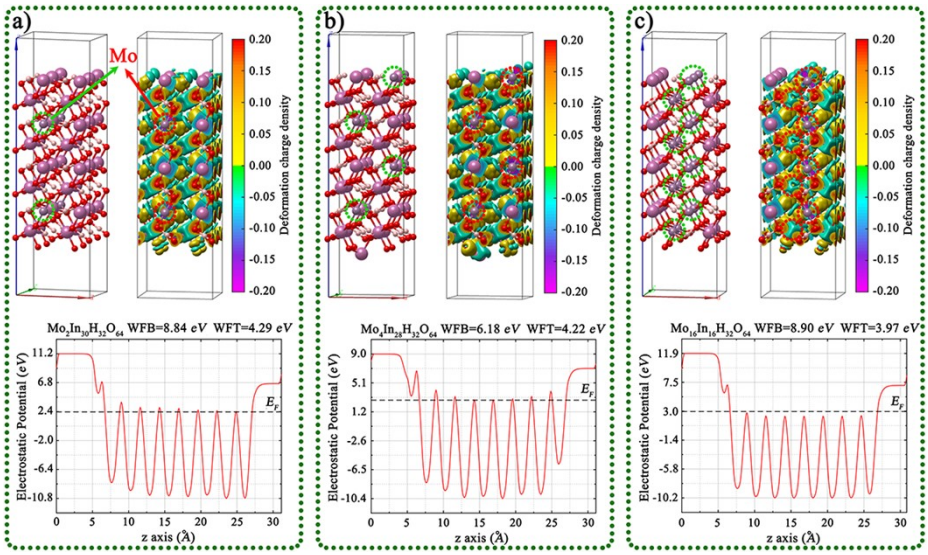

Figure S18. Geometric structures, charge density difference, calculated Fermi levels, and work functions of the (001) surface of (a) $Mo_2In_{30}H_{32}O_{64}$, (b) $Mo_4In_{28}H_{32}O_{64}$, and (c)

$Mo_{16}In_{16}H_{32}O_{64}$.

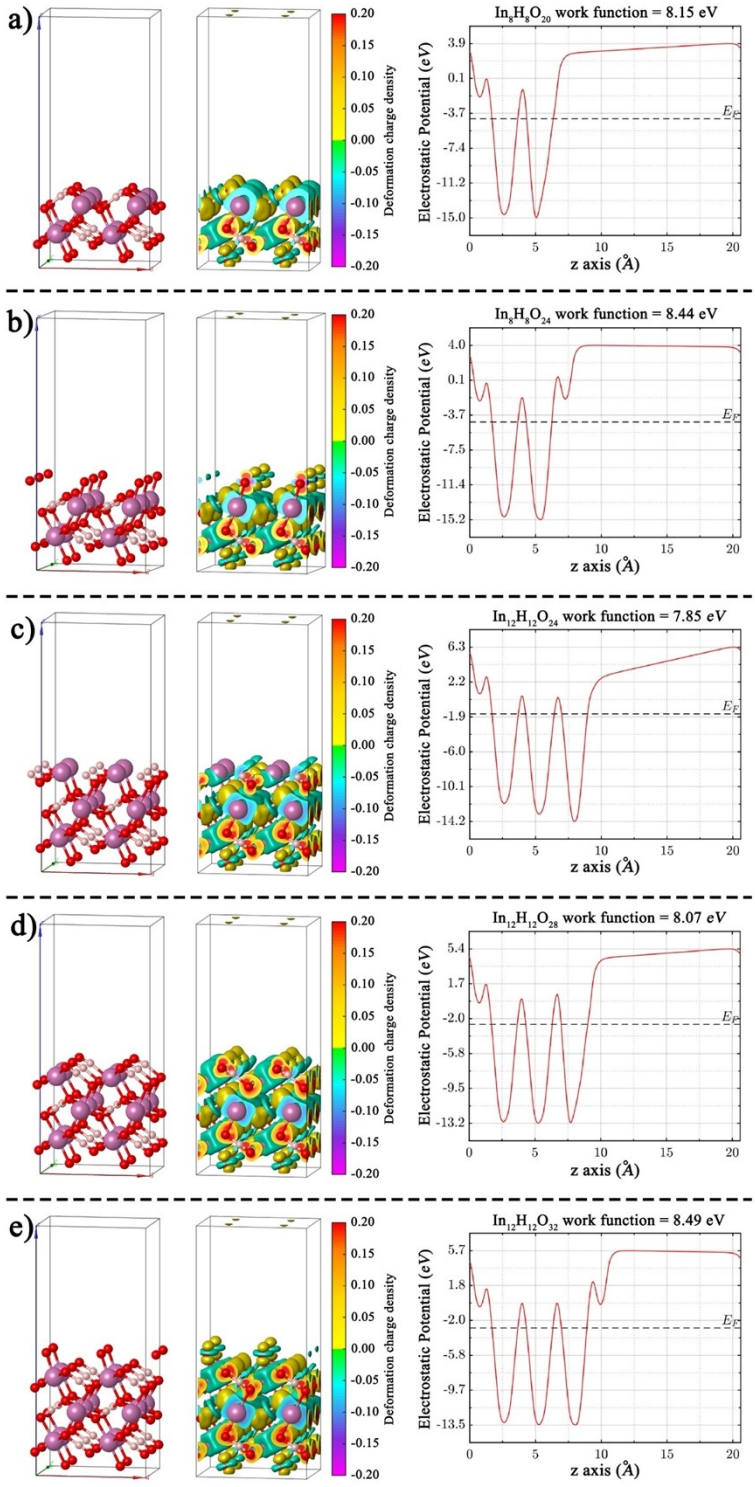

Figure S19. Geometric structures, charge density difference, calculated Fermi levels, and work functions of the (001) surface of InOOH with different section thicknesses and different exposed atoms.

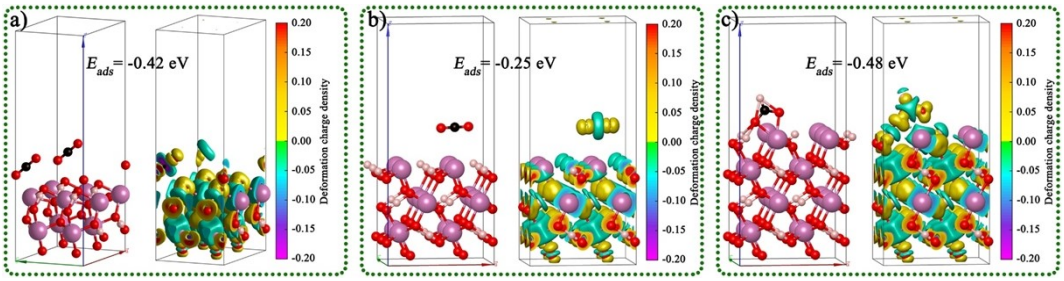

Figure S20. The geometric structures and calculated adsorption energies (E_{ads}) of CO_2 on the InOOH (001) surface with different section thickness, differently exposed atoms, and different CO_2 adsorption positions.

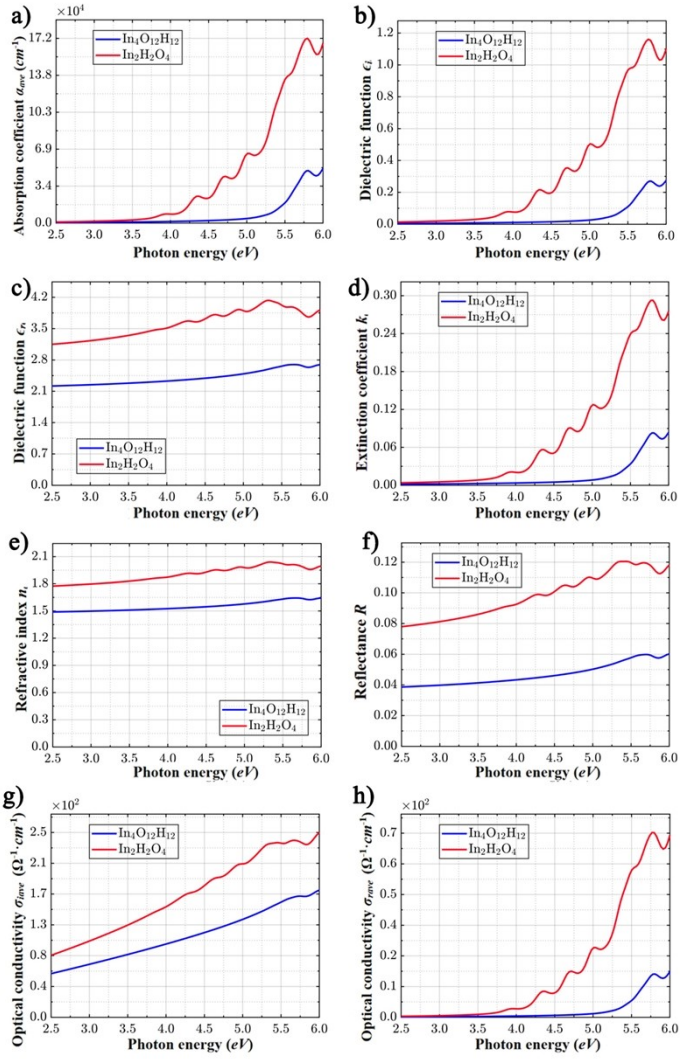

Figure S21. Theoretical simulation of optical properties for $In_4O_{12}H_{12}$ and $In_2H_2O_4$: (a) Absorption coefficient, (b,c) Dielectric function, (d) Extinction coefficient, (e) Refractive index, f) Reflectance, and (g,h) Optical conductivity.

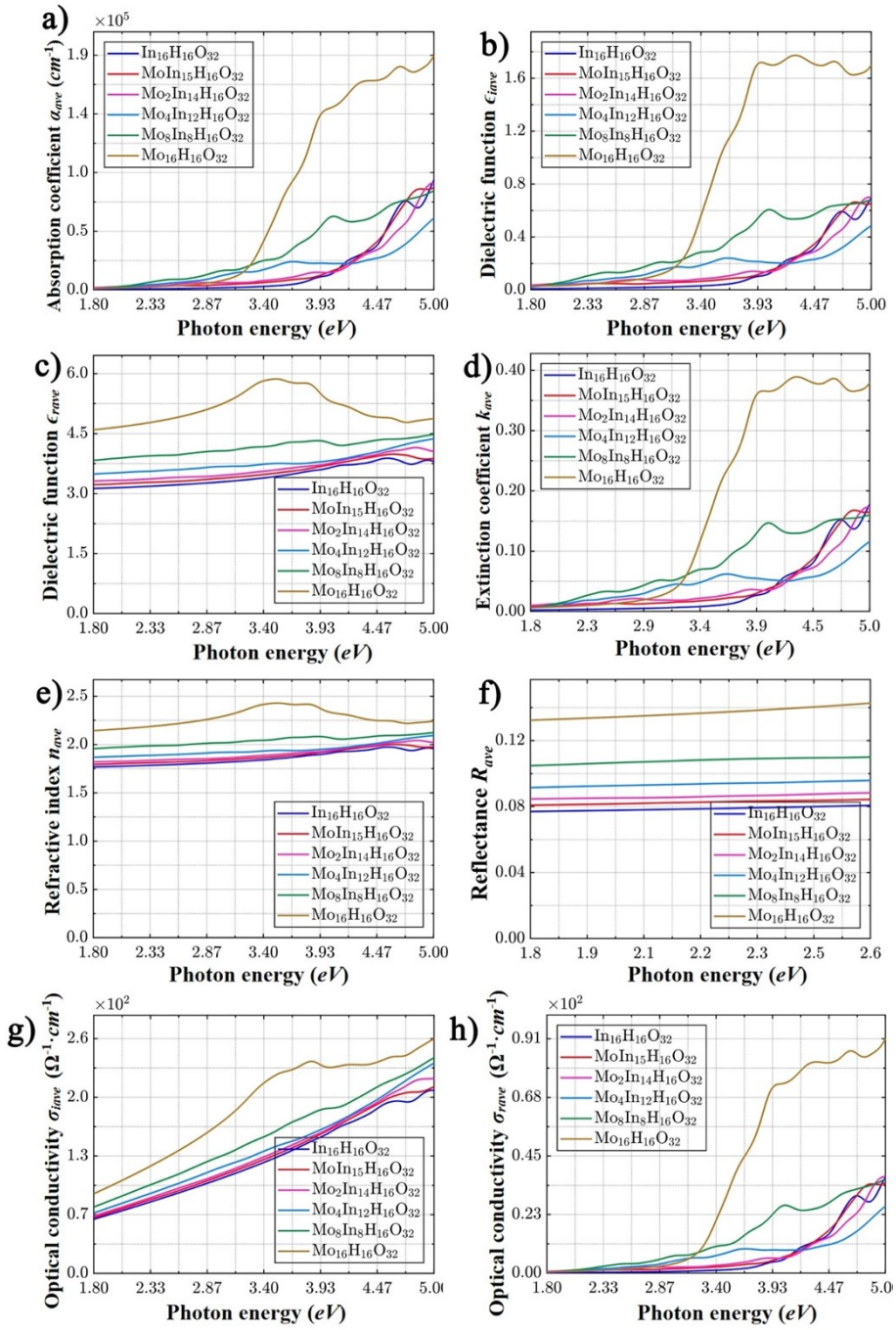

Figure S22. Theoretical simulation of optical properties for $In_{16}H_{16}O_{32}$, $MoIn_{15}H_{16}O_{32}$, $Mo_2In_{14}H_{16}O_{32}$, $Mo_4In_{12}H_{16}O_{32}$, $Mo_8In_8H_{16}O_{32}$, and $Mo_{16}H_{16}O_{32}$: (a) Absorption coefficient, (b,c) Dielectric function, (d) Extinction coefficient, (e) Refractive index, (f) Reflectance, and (g,h) Optical conductivity.